$p_{x,y}$-orbital counterpart of graphene: Cold atoms in the honeycomb optical lattice

Congjun Wu[1] and S. Das Sarma[2]
[1]*Department of Physics, University of California, San Diego, California 92093, USA*
[2]*Condensed Matter Theory Center, Department of Physics, University of Maryland, College Park, Maryland 20742, USA*
(Received 27 December 2007; revised manuscript received 12 May 2008; published 11 June 2008)

We study the ground-state properties of the interacting spinless fermions in the $p_{x,y}$-orbital bands in the two-dimensional honeycomb optical lattice, which exhibit different features from those in the p_z-orbital system of graphene. In addition to two dispersive bands with Dirac cones, the tight-binding band structure exhibits another two completely flat bands over the entire Brillouin zone. With the realistic sinusoidal optical potential, the flat bands acquire a finite but much smaller bandwidth compared to the dispersive bands. The band flatness dramatically enhanced interaction effects giving rise to various charge and bond ordered states at commensurate fillings of $n=\frac{i}{6}$ $(i=1-6)$. At $n=\frac{1}{6}$, the many-body ground states can be exactly solved as the close-packed hexagon states which can be stabilized even in the weakly interacting regime. The dimerization of bonding strength occurs at both $n=\frac{1}{2}$ and $\frac{5}{6}$, and the latter case is accompanied with the charge-density wave of holes. The trimerization of bonding strength and charge inhomogeneity appear at $n=\frac{1}{3},\frac{2}{3}$. These crystalline orders exhibit themselves in the noise correlations of the time-of-flight spectra.

DOI: 10.1103/PhysRevB.77.235107 PACS number(s): 03.75.Ss, 03.75.Nt, 05.50.+q, 73.43.Nq

I. INTRODUCTION

There has been tremendous progress during the past decade in cold atom physics. In the early days, Bose-Einstein condensation was first realized in magnetic traps by using dilute alkali atoms,[1,2] where interaction effects are weak. Later on, important achievements have been made to realize strongly correlated systems by using optical lattices. The major advantage of optical lattices is the excellent controllability of interaction strength. For example, the superfluid to Mott insulator transition of bosons has been experimentally observed.[3] Recently, cold atom physics in optical lattices is merging with condensed-matter physics, which provides a wonderful opportunity to explore new states of matter.

An important aspect of strongly correlated systems is orbital physics, which studies an additional degree of freedom independent of charge and spin. In many transition-metal oxides, the *d* orbitals are partially filled, which enables the orbital degree of freedom to be active. Orbital physics is characterized by orbital degeneracy and spatial anisotropy of orbital orientation. The interplay between orbital, spin, and charge degrees of freedom gives rise to many interesting phenomena such as metal-insulator transitions, superconductivity, and colossal magnetoresistance.[4–6]

Orbital degrees of freedom also exist in optical lattices. Although most of current research of cold fermions and bosons focuses on the lowest *s*-orbital bands, large progress has been made in high orbital bands. An important advantage of optical lattices is the rigidity of lattices. They are free from the Jahn-Teller-type lattice distortion which often occurs in transition-metal oxides and quench the orbital degrees of freedom. Orbital physics in optical lattices exhibits other features which are not usually realized in solid-state systems. Recently, the properties of bosons in the first-excited *p*-orbital bands have been attracting a great deal of attention.[7–14] Scarola and Das Sarma[7] proposed to realize the supersolid state by using bosons in the high orbitals to generate the next-nearest-neighbor interaction. Isacsson and Girvin[8] investigated the subextensive Z_2 symmetry of the *p*-orbital bosons in the square lattice and its consequential nematic superfluidity. Liu and Wu[9] and Kuklov[10] studied the antiferromagnetic ordering of the on-site orbital angular-momentum moment. It was also proposed in Ref. 9 to enhance the lifetime of *p*-orbital bosons by using a Bose-Fermi mixture to reduce the available phase space of decay process of bosons. Wu *et al.*[11] further investigated the superfluid and Mott-insulating states of *p*-orbital bosons in the frustrated triangular lattice and found a novel stripe phase of orbital angular momentums. Xu and Fisher[12] studied a model of bond algebraic liquid phase and phase transitions in the anisotropic *xy* models[13] in the context in the *p*-orbital boson systems.

On the experimental side, the progress of orbital physics with cold atoms has also been truly exciting, which opens up the new opportunity to study orbital physics. Browaeys *et al.*[15] and Kohl *et al.*[16] demonstrated the population of high orbital bands with both bosons and fermions. Furthermore, Sebby-Strabley *et al.*[17] successfully pumped bosons into the excited bands in the double-well lattice. More recently, exciting progress has been made by Muller *et al.*[18] to realize the metastable *p*-orbital boson systems by using the stimulated Raman transition to pump bosons to high orbital bands. The spatially anisotropic phase coherence pattern has been observed in the time-of-flight (TOF) experiments. This opens up an experimental direction to investigate condensates of bosons in the excited *p* bands.

On the other hand, fermions in the *p*-orbital bands also possess interesting behaviors.[19–22] Recently, Wu *et al.*[19] studied the flat band structure in the $p_{x,y}$-orbital physics in the honeycomb lattice. Compared to the p_z-orbital system of graphene, which has been attracting tremendous attention since the discovery of the quantum Hall effect therein,[23–25] the $p_{x,y}$-orbital honeycomb systems exhibit even richer physics. In graphene, the active bands near the Fermi energy are "π" type, composed of the p_z orbital directly normal to the graphene plane, thus graphene is not a good system to inves-

tigate orbital physics. In contrast, it is the other two p orbitals ($p_{x,y}$) that lie in plane and exhibit both orbital degeneracy and spatial anisotropy, giving rise to the interesting flat band physics.[19] In solid-state systems of graphene and MgB_2, $p_{x,y}$ orbitals hybridize with the s orbital, resulting in the σ-bonding (the sp^2 hybridization) band. This σ band is fully filled and inert in graphene but is partly filled and contributes to the two-band superconductivity in MgB_2.[26] Due to the large s-orbital component, the essential feature of orbital physics, orbital anisotropy, is not prominent in these two systems. In contrast, the $p_{x,y}$-orbital bands in optical lattices are well separated from the s band with negligible hybridization, providing a unique opportunity to study the pure $p_{x,y}$-orbital physics in the honeycomb lattice. This research will provide us another perspective in the honeycomb lattice and is complementary to the recent research focus on the single band system of graphene. Other works of the p-orbital fermions include the investigation of orbital exchange physics in the Mott-insulating states finding various orbital ordering and frustration behaviors[20,22] and the study of the possibility to enhance the antiferromagnetic ordering of fermions in the p orbital of three-dimensional cubic lattices.[21]

Interaction effects in the $p_{x,y}$-orbital honeycomb optical lattices can be much stronger than those in the p_z-orbital graphene systems. In real graphene the dimensionless coupling constant $r_s=e^2/(\epsilon\hbar v)$ has a maximum value of 2.3 in vacuum (and $r_s<1$ for the current available graphene samples on SiO_2 or SiC substrates), taking $v=10^6$ cm/s. Thus graphene is very far from the $r_s=39$ regime needed for Wigner crystallization.[27] Much of graphene interaction physics is described by perturbative weak-coupling renormalizations of the quasiparticle spectral function, as shown both theoretically and experimentally.[28–30] Furthermore, real graphene physics is complicated by electron-phonon interactions.[31] In contrast, in the $p_{x,y}$-orbital honeycomb lattice systems, the flat band quenches the kinetic energy, and thus interaction physics is nonperturbative and generic, leading to qualitatively orbital physics phenomena, e.g., Wigner-Mott physics, which can show up easily.[19]

This paper works as an expanded version of a previous publication of Ref. 19, with results and all the theoretical details of the behavior of spinless fermions in the $p_{x,y}$-orbital bands in the honeycomb lattice. The current work is motivated by considerations of using the optical lattices to go beyond what can be achieved in solid-state systems, i.e., obtain exotic strongly correlated orbital quantum phases which have not yet been studied in condensed-matter physics. The paper is organized as follows. In Sec. II, we analyze the band structures in both the simplified tight-binding model and the realistic optical potential constructed from three coplanar laser beams.[32] The band structures contain both Dirac cones in two dispersive bands and other two nearly flat bands over the entire Brillouin zone (BZ) whose flatness becomes exact if the π bonding is neglected. Special attention is paid for the orbital configurations of the localized Wannier-type eigenfunctions in the flat bands and also at the Dirac points. In Sec. III, the interacting Hamiltonian is introduced and methods of enhancing the Hubbard-type on-site interaction are proposed. In Sec. IV, the interaction effect in the partially filled flat band is discussed. The situation is somewhat analogous to that in the fractional quantum Hall effect of electrons in the lowest Landau level. When the flat band is partially filled, the effects of interactions are entirely nonperturbative. We obtain the *exact* many-body plaquette Wigner-crystal state at filling $\langle n\rangle=\frac{1}{6}$, which is the close-packed hexagon state and is stable even in the weak-interaction regime. In Sec. V, we present various charge and bond ordered states, including dimerized and trimerized states at higher commensurate fillings in the strong-interaction regime. In Sec. VI, the noise correlation in the time-of-flight experiments is discussed. Conclusions and outlook for future research are discussed in Sec. VII.

II. $p_{x,y}$-ORBITAL BAND STRUCTURE IN THE HONEYCOMB LATTICE

In this section, we will give a detailed analysis to the $p_{x,y}$-orbital band structure in the two-dimensional (2D) honeycomb lattice which is featured by the interesting properties of both flat bands and Dirac cones. We will first discuss the experimental construction of such a lattice and then solve the band structure by using both the simplified tight-binding model and the realistic sinusoidal optical potential.

A. Construction of the optical honeycomb lattice

The honeycomb optical lattice was realized experimentally by using three laser beams with coplanar propagating wave vectors $\vec{q}_i (i=1\sim3)$ quite some time ago.[32] The magnitudes of these wave vectors are the same and their directions form an angle of 120° with each other. Assuming that the polarizations of the electric fields of the three beams are all along the z direction, the optical potential distribution can be expressed as

$$V(\vec{r}) = V_0 \sum_{i=1-3} \cos(\vec{p}_i \cdot \vec{r}), \tag{1}$$

where $\vec{p}_1=\vec{q}_2-\vec{q}_3$, $\vec{p}_2=\vec{q}_3-\vec{q}_1$, and $\vec{p}_3=\vec{q}_1-\vec{q}_2$. In the case of blue detuning, V_0 is positive and the potential minima form a hexagonal lattice, as depicted in Fig. 1. In contrast, the red detuning laser beams generate a 2D triangular lattice. In both cases, the lattice is topologically stable against the phase drift of the laser beams, which only causes an overall shift but not the distortion of the lattice. Figure 1(b) depicts the potential distribution in one unit cell of the honeycomb lattice, where a potential maximum locates in the center and six potential minima sit around. Without loss of any generality, we take $\vec{p}_{1,2}=p(\pm\frac{\sqrt{3}}{2}\hat{e}_x+\frac{1}{2}\hat{e}_y)$ and $\vec{p}_3=-p\hat{e}_y$, where $p=\frac{4\pi}{3a}$ and a is the distance between the nearest-neighbor site in the honeycomb lattice. We define the recoil energy in such a lattice system as $E_r=\frac{\hbar^2p^2}{2m}$, where m is the mass of the atom.

B. Tight-binding model

The optical potential around the center of each site is approximately an anisotropic harmonic well. We assume that the vibration frequencies along the x, y, and z directions satisfy $\omega_z \gg \omega_x=\omega_y=\omega_{xy}$, and thus the energy of the p_z orbital is much higher than that of the $p_{x,y}$-orbital bands. When the

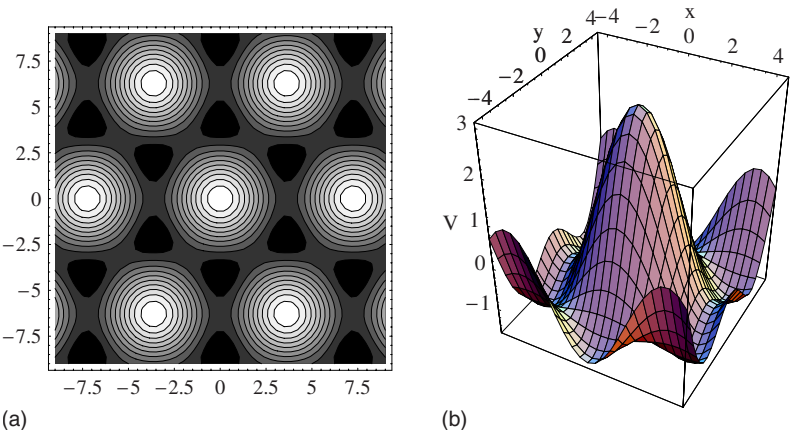

FIG. 1. (Color online) (a) The contour plot of the optical potential of the 2D honeycomb lattice described by Eq. (1). (b) The optical potential distribution around the potential maximum in one unit cell.

lowest s band is fully filled and thus inert, the active orbital bands will be of the $p_{x,y}$. Due to the spatial orientation of the p orbitals, the hopping processes in the p orbitals can be classified into the σ- and π-type bondings. The former describes the hopping between p orbitals on neighboring sites with the orientation along the bond direction, while the latter describes the hopping between p orbitals perpendicular to the bond direction. In other words, the σ bonding is of the "head to tail" type, while the π bonding is of the "shoulder by shoulder" type. Typically, the amplitude of the π bonding is much smaller than that of the σ bonding because of the strong orientational anisotropy.

The structure of the honeycomb lattice is depicted in Fig. 2(a). Each unit cell in the honeycomb lattice contains two sites depicted as A and B. We define three unit vectors from site A to its three neighboring sites B as

$$\hat{e}_{1,2} = \pm \frac{\sqrt{3}}{2}\hat{e}_x + \frac{1}{2}\hat{e}_y, \quad \hat{e}_3 = -\hat{e}_y \tag{2}$$

and their differences $\vec{b}_i = \frac{1}{2}\epsilon_{ijk}(\hat{e}_j - \hat{e}_k)$ as

$$\vec{b}_3 = \sqrt{3}\hat{e}_x, \quad \vec{b}_{1,2} = -\frac{\sqrt{3}}{2}\hat{e}_x \pm \frac{3}{2}\hat{e}_y. \tag{3}$$

The projections of the p orbitals along the $\hat{e}_{1,2,3}$ directions are defined as

$$p_{1,2} = \pm \frac{\sqrt{3}}{2}p_x + \frac{1}{2}p_y, \quad p_3 = -p_y. \tag{4}$$

Only two of them are linearly independent. In the realistic optical potential depicted in Fig. 1(a), the potential distribution inside each optical site is only approximately isotropic in the xy plane. Away from the center, the potential exhibits a threefold rotational anisotropy. The point-group symmetry with respect to the center of each site is reduced into C_{3V} including the threefold rotation and reflection. Nevertheless, as required by this symmetry, $p_{x,y}$ remain degenerate and each of $p_{1,2,3}$ defined above is still an on-site eigenstate with the orientation along the corresponding bond direction. However, they are no longer purely parity odd due to the breaking of the inversion symmetry with respect to the center of each optical site. (The overall inversion symmetry with respect to the center of each potential maximum is still preserved, but this involves the transformation among different sites.)

The σ-bonding part in the kinetic energy reads

$$H_0 = t_\parallel \sum_{\vec{r}\in A, i=1-3} \{p^\dagger_{\vec{r},i} p_{\vec{r}+a\hat{e}_i,i} + \text{H.c.}\} - \mu \sum_{\vec{r}\in A\oplus B} n_{\vec{r}}, \tag{5}$$

where the summation over $\vec{r}$ in the first term is only on the A sublattice, a is the nearest-neighbor distance, and $n_{\vec{r}} = n_{\vec{r},x} + n_{\vec{r},y}$ is the total particle number in both p_x and p_y orbitals at the site $\vec{r}$. $t_\parallel$ is positive due to the dominant odd-parity component of the p orbitals and is set to 1 below. Equation (5) neglects the much smaller π-bonding $t_\perp$ terms which in principle exist, and their effects will be discussed in Sec. II E.

Next we discuss the spectrum of the tight-binding Hamiltonian [Eq. (5)]. In momentum space, we define a four-component spinor as

$$\psi(\vec{k}) = [p_{Ax}(\vec{k}), p_{Ay}(\vec{k}), p_{Bx}(\vec{k}), p_{By}(\vec{k})]^T, \tag{6}$$

where each component is the Fourier transform of the $p_{x,y}$ orbit in site A or B. Then Eq. (5) becomes

$$H_0 = t_\parallel \sum_k \psi^\dagger_\alpha(\vec{k})\{H_{\alpha\beta}(\vec{k}) - \mu\delta_{\alpha\beta}\}\psi_\beta(\vec{k}), \tag{7}$$

where the matrix kernel $H_{\alpha\beta}(\vec{k})$ takes the structure as

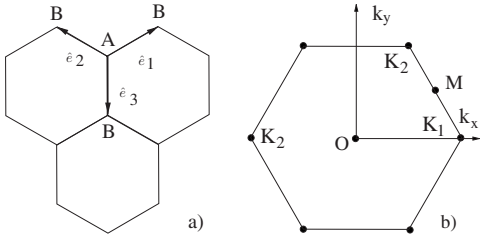

FIG. 2. (a) The two sublattice structure (A and B) of the honeycomb lattice. (b) The hexagon Brillouin zone with edge length $4\pi/(3\sqrt{3}a)$.

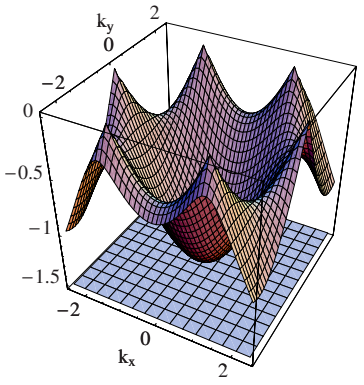

FIG. 3. (Color online) Dispersion of the two-lowest $p_{x,y}$-orbital bands $E_{1,2}$. The band E_1 is completely flat, while E_2 exhibits Dirac points at $K_{1,2}=(\pm\frac{4\pi}{3\sqrt{3}a},0)$. The other two bands are symmetric with respect to $E=0$ [from Wu *et al.* (Ref. 19)].

$$\begin{pmatrix} 0 & 0 & \frac{3}{4}(e^{i\vec{k}\cdot\vec{e}_1}+e^{i\vec{k}\cdot\vec{e}_2}) & \frac{\sqrt{3}}{4}(e^{i\vec{k}\cdot\vec{e}_1}-e^{i\vec{k}\cdot\vec{e}_2}) \\ 0 & 0 & \frac{\sqrt{3}}{4}(e^{i\vec{k}\cdot\vec{e}_1}-e^{i\vec{k}\cdot\vec{e}_2}) & \frac{1}{4}(e^{i\vec{k}\cdot\vec{e}_1}+e^{i\vec{k}\cdot\vec{e}_2})+e^{i\vec{k}\cdot\vec{e}_3} \\ \text{H.c.} & & 0 & 0 \\ & & 0 & 0 \end{pmatrix}.$$

Its spectrum is symmetric with respect to zero because the sign of the $t_\parallel$ term can be flipped by changing the sign of the $p_{x,y}$ orbitals in one sublattice but not the other. The dispersion relations of the four bands read

$$E_{1,4}=\mp\frac{3}{2}t_\parallel,\quad E_{2,3}=\mp\frac{t_\parallel}{2}\sqrt{3+2\sum_i\cos\vec{k}\cdot\vec{b}_i}, \tag{8}$$

as shown in Fig. 3. Interestingly, the band structure exhibits two flat bands $E_{1,4}$ over the entire 2D Brillouin zone. The corresponding eigenvectors can be found analytically as

$$\psi_{1,4}(\vec{k})=\frac{1}{\sqrt{N_0(\vec{k})}}\left\{\frac{1}{\sqrt{3}}[f_{23}^*(\vec{k})-f_{31}^*(\vec{k})],\ -f_{12}^*(\vec{k}),\right.$$
$$\left.\pm\frac{1}{\sqrt{3}}[f_{23}(\vec{k})-f_{31}(\vec{k})],\ \mp f_{12}(\vec{k})\right\}^T, \tag{9}$$

where $f_{ij}=e^{i\vec{k}\cdot\hat{e}_i}-e^{i\vec{k}\cdot\hat{e}_j}$ and the normalization factor reads

$$N_0(\vec{k})=\frac{8}{3}\left(3-\sum_i\cos\vec{k}\cdot\vec{b}_i\right). \tag{10}$$

On the other hand, the $E_{2,3}$ bands are dispersive exhibiting the Dirac cone structure, whose bandwidth is determined by $t_\parallel$. We construct a set of basis which is orthogonal to $\psi_{1,4}(\vec{k})$ and spans the subspace for the $E_{2,3}$ bands as

$$\phi(\vec{k})=\sqrt{\frac{2}{N_0}}\left\{f_{12}(\vec{k}),\quad\frac{1}{\sqrt{3}}[f_{23}(\vec{k})-f_{31}(\vec{k})],\ 0,\ 0\right\},$$

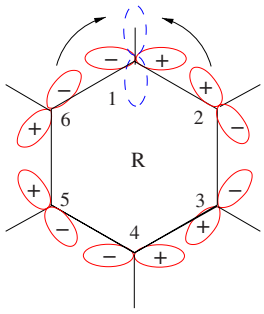

FIG. 4. (Color online) The Wannier-type localized eigenstate for the lowest band. The orbital configuration at each site is oriented along a direction tangential to the closed loop on which the particle is delocalized. The absence of the π hopping and the destructive interference together ensure such a state as an eigenstate.

$$\phi'(\vec{k})=\sqrt{\frac{2}{N_0}}\left\{0,\ 0,\ f_{12}^*(\vec{k}),\quad\frac{1}{\sqrt{3}}[f_{23}^*(\vec{k})-f_{31}^*(\vec{k})]\right\}. \tag{11}$$

Then the Hamiltonian becomes the same as in graphene,

$$H_{23}(\vec{k})=-\frac{t_\parallel}{2}\begin{pmatrix} 0 & \sum_i e^{-i\vec{k}\cdot\hat{e}_i} \\ \sum_i e^{i\vec{k}\cdot\hat{e}_i} & 0 \end{pmatrix}. \tag{12}$$

Two Dirac cones appear at $K_{1,2}=(\pm\frac{4\pi}{3\sqrt{3}a},0)$. The eigenvectors of the bands $E_{2,3}(\vec{k})$ read

$$\psi_{2,3}(\vec{k})=\frac{1}{\sqrt{2}}\{\phi(\vec{k})\pm e^{i\theta_k}\phi'(\vec{k})\}, \tag{13}$$

with the angle of $\theta_{\vec{k}}$

$$\theta_k=\arg\left(\sum_i e^{i\vec{k}\cdot\hat{e}_i}\right). \tag{14}$$

C. Localized eigenstates

The complete flatness of the $E_{1,4}$ bands means that these eigenstates can be represented as a linear superposition of a set of degenerate *localized* states. The construction of this localized state is depicted in Fig. 4. For each hexagon plaquette denoted by its center position $\vec{R}$, there exists one such eigenstate for the bottom band E_1,

$$|\psi_{\vec{R}}\rangle=\sum_{j=1}^{6}(-)^{j-1}\{\cos\theta_j|p_{j,x}\rangle-\sin\theta_j|p_{j,y}\rangle\}, \tag{15}$$

where j is the site index and $\theta_j=(j-1)\frac{\pi}{3}$. The localized eigenstates of the E_4 band can be obtained by flipping the signs of the p orbits on sites 2, 4, and 6 and keeping those on sites 1, 3, and 5 unchanged. The p-orbital configuration on each site is perpendicular to the links external to the hexagonal loop, thus the σ bonding forbids the particle to directly hop outside through these links. Furthermore, the amplitudes for the particle to hop to the p orbital in the radial direction

from the neighboring sites vanish due to the destructive interference, as shown in Fig. 4. The particle is trapped in the plaquette without "leaking" to the outside, and thus $|\psi_{\vec{R}}\rangle$ is the eigenstate with the energy of E_1. The states $|\psi_{\vec{R}}\rangle$ are all linearly independent apart from one overall constraint $\Sigma_{\vec{R}}|\psi_{\vec{R}}\rangle=0$ under periodic boundary conditions. The localized states on two neighboring edge-sharing plaquettes are not orthogonal to each other.

The Bloch wave states in the flat band E_1 are constructed as

$$|\psi_{1,k}\rangle = \frac{1}{\sqrt{N_k}}\sum_k e^{i\vec{k}\cdot\vec{R}}|\psi_{\vec{R}}\rangle \quad [\vec{k}\neq(0,0)]. \tag{16}$$

The doubly degenerate eigenstate at $\vec{k}=(0,0)$ cannot be constructed from the above plaquette states. They are $|\psi_{\vec{k}=(0,0)}\rangle_{1,2}=\Sigma_{\vec{r}\in A}|p_{x(y),\vec{r}}\rangle-\Sigma_{\vec{r}\in B}|p_{x(y),\vec{r}}\rangle$.

D. Orbital configuration at $\vec{k}=(0,0)$ and $K_{1,2}$

The major difference between the physics of $p_{x,y}$-orbital bands and that of graphene is the orbital degree of freedom. The orbital configuration for each band varies as lattice momentum $\vec{k}$ changes in the Brillouin zone. Around the center of the Brillouin zone $\vec{k}=(0,0)$, the Hamiltonian can be expanded as

$$H = \frac{3}{2}\tau_1\otimes I - \frac{3}{4}k_y\tau_2\otimes\sigma_3 - \frac{3}{4}k_x\tau_2\otimes\sigma_1, \tag{17}$$

where Pauli matrices $\sigma_{1,2,3}$ describe the $p_{x,y}$-orbital degrees of freedom and $\tau_{1,2,3}$ describe the sublattices A,B degrees of freedom. The eigenvectors of $\psi_{1,2,3,4}$ can be approximated as

$$\psi_{1,4}(\vec{k}) = \frac{1}{\sqrt{2}|k|}\{-k_y,k_x,\pm k_y,\mp k_x\},$$

$$\psi_{2,3}(\vec{k}) = \frac{1}{\sqrt{2}|k|}\{k_x,k_y,\mp k_x,\mp k_y\}. \tag{18}$$

Thus around $\vec{k}=(0,0)$, the orbital configuration is polarlike, i.e., a real combination of $p_{x,y}$. The orbital orientation in each site is either parallel or perpendicular to $\vec{k}$.

Now let us investigate the orbital configurations around the vertices of $K_{1,2}$ of the Brillouin zone. Around K_1, the Hamiltonian can be expanded as

$$H(\vec{k}) = -\frac{3}{4}\Delta k_x\tau_1\otimes I + \frac{3}{4}\Delta k_y\tau_2\otimes I - \left(\frac{3}{4}+\frac{3}{8}\Delta k_x\right)\tau_1\otimes\sigma_3 - \frac{3}{8}\Delta k_y\tau_2\otimes\sigma_3 - \frac{3}{8}\Delta k_y\tau_1\otimes\sigma_1 - \left(\frac{3}{4}-\frac{3}{8}\Delta k_x\right)\tau_2\otimes\sigma_1, \tag{19}$$

where $\Delta\vec{k}=\vec{k}-\vec{K}_1$ and $g_\pm(\vec{k})=\Delta k_x\pm i\Delta k_y$. The eigenvectors of the flat bands $E_{1,4}$ can be approximated as

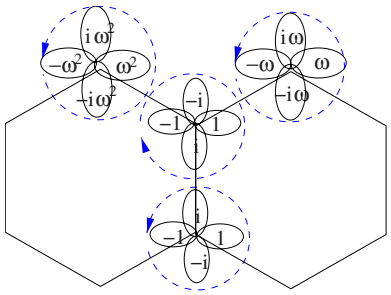

a) Ψ_1

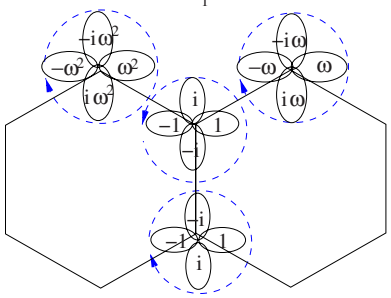

b) Ψ_2

FIG. 5. (Color online) The orbital configurations of eigenstates at K_1, which are of $p_x\pm ip_y$ type. The phase of each lobe is presented ($\omega=e^{i(2\pi/3)}$). (a) $\psi_1(\vec{K}_1)$ ($E_1=-\frac{3}{2}t_\parallel$). (b) $\psi_2(\vec{K}_1)$ with $\alpha_k=0$ ($E_2=0$).

$$\psi_{1,4}(\vec{k}) = \frac{1}{2}\left\{1+\frac{g_+(\vec{k})}{2}, \quad -i\left[1-\frac{g_+(\vec{k})}{2}\right], \pm\left[1+\frac{g_-(\vec{k})}{2}\right], \quad \pm i\left[1-\frac{g_-(\vec{k})}{2}\right]\right\}^T. \tag{20}$$

Similarly, the eigenvectors of the dispersive bands $E_{2,3}$ are approximated as

$$\psi_{2,3}(\vec{k}) = \frac{1}{2}\left\{1-\frac{g_-(\vec{k})}{2}, \quad i\left(1+\frac{g_-(\vec{k})}{2}\right), \pm e^{i\alpha_k}\left(1-\frac{g_+(\vec{k})}{2}\right), \quad -i\left(1+\frac{g_+(\vec{k})}{2}\right)\right\}^T, \tag{21}$$

where α_k is the angle defined in Eq. (14). Thus the orbital configuration at $\vec{k}=\vec{K}_1$ on each site is the axial state $p_x\pm ip_y$, as depicted in Fig. 5. This is in contrast to the polar configuration at $\vec{k}=(0,0)$. The orbital configuration at $\vec{k}=\vec{K}_2$ can be obtained by performing time-reversal transformation.

E. π-bonding term and other perturbations

The π-bonding term in principle exists in the realistic optical lattices. We define the projections of $p_{x,y}$ orbitals perpendicular to the $\hat{e}_{1,2,3}$ directions as

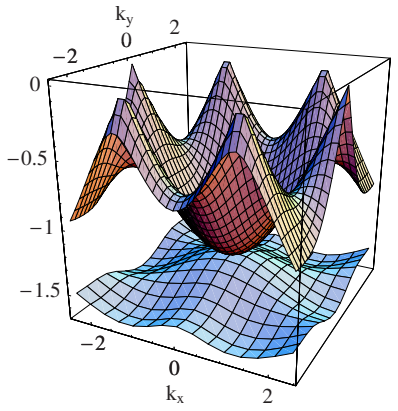

FIG. 6. (Color online) Dispersion of the two-lowest $p_{x,y}$-orbital bands $E_{1,2}$ in the presence of the π-bonding $t_\perp$. The bottom band is no longer rigorously flat but acquires a narrow width of $t_\perp$.

$$p'_{1,2} = -\frac{1}{2}p_x \pm \frac{\sqrt{3}}{2}p_y, \quad p'_3 = p_x. \tag{22}$$

The π-bonding term can be written as

$$H_\pi = -t_\perp \sum_{\vec{r}\in A, i=1-3} \{p'^{\dagger}_{\vec{r},i} p'_{\vec{r}+a\hat{e}_i,i} + \text{H.c.}\}. \tag{23}$$

Please note that the hopping integral of the π bonding has the opposite sign to that of the σ bonding. In this case, the bottom and top bands $E_{1,4}$ are no longer rigorously flat but develop a narrow width $3t_\perp$, as depicted in Fig. 6. The E_1 and E_2 bands still touch at the center of the Brillouin zone. This can be understood from the structure of the localized eigenstates in Fig. 4. The π-bonding term causes the particle leaking off the plaquette and thus correspondingly develops the bandwidth. Nevertheless we will show in Sec. II F that in the realistic optical potential such an effect is negligibly small.

Next we discuss the case that the A and B sites are with different on-site potentials. In the graphenelike systems, this corresponds to a mass term in the Dirac point. In the $p_{x,y}$-orbital systems, such a term can be described as

$$H = \Delta E \left\{ \sum_{\vec{r}\in A} n_{\vec{r}} - \sum_{\vec{r}\in B} n_{\vec{r}} \right\}. \tag{24}$$

The spectrum is depicted in Fig. 7 with the opening of a gap of ΔE in the Dirac points as usual. Interestingly, the flat band feature remains unchanged. This can be understood in terms of the localized eigenstate picture. In this case, the localized eigenstates of the E_1 band still possess a similar configuration as in Fig. 4, but their wave functions distribute with different weights on A and B sublattices.

F. Band structure from the continuum optical potential

We numerically calculate the band structure in the realistic optical potential of Eq. (1). The band Hamiltonian becomes

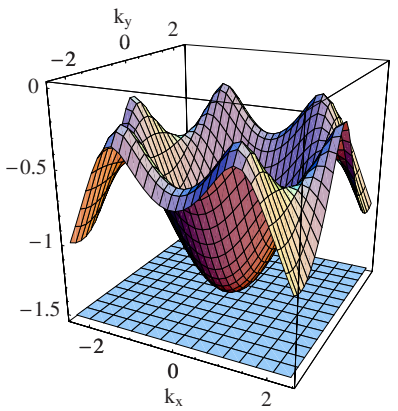

FIG. 7. (Color online) Dispersion of the two-lowest $p_{x,y}$-orbital bands $E_{1,2}$ in the presence of the on-site potential.

$$H = -\frac{\hbar^2 \nabla_r^2}{2m} + V_0 \sum_{i=1-3} \cos(\vec{p}_i \cdot \vec{r}). \tag{25}$$

Since this is a nonsingular sinusoidal potential, we use the plane-wave basis to calculate the matrix elements $\langle \vec{k}|H|\vec{k}'\rangle$, where $\vec{k}' = \vec{k} \pm \vec{p}_i$ $(i=1-3)$. For each $\vec{k}$ in the Brillouin zone, we truncate the matrix up to the 120 plane-wave basis, which should be sufficient for the lowest several bands.

The band dispersions along the path from O to K_1, M, and K_2 are depicted in Fig. 8. The locations of O, $K_{1,2}$, and M in the Brillouin zone are depicted in Fig. 2. The lowest two bands are of the s orbital exhibiting Dirac cones at K_1 and K_2. The next four are of the $p_{x,y}$ orbitals. The band flatness is largely preserved even with the realistic optical potential of Eq. (1). In Fig. 8(a) with $V/E_r = 5$, the bottom one of the four p-orbital bands is nearly flat with the width of $7 \times 10^{-3} E_r$ which is only 2% of that of the second one which is $0.35E_r$. The width of the top band is $4 \times 10^{-2} E_r$ which is still small but considerably larger than that of the bottom one. The third band is the widest one with the width of $0.62E_r$. As we can see, the particle-hole symmetry in the tight-binding model is no longer kept because of the unavoidable hybridization with other bands and long-range hoppings. The spectra become more symmetric with a strong optical potential, as shown in Fig. 8(b) $(V/E_r = 10)$ in which the tight-binding model is a better approximation and long-range hoppings can be neglected. The widths of the beginning six bands (the s- and $p_{x,y}$-orbital bands) as a function of the V_0/E_r are depicted in Fig. 9.

III. INTERACTIONS IN THE $p_{x,y}$-ORBITAL SPINLESS FERMIONS

In the following, we will mainly consider interacting spinless fermions in the $p_{x,y}$-orbital bands in the honeycomb lattices and leave the research for spinful fermions to future publications. The preparation of spinless fermions can be controlled by cooling the system in the external Zeeman field. Due to the lack of a spin-relaxation mechanism in cold atom systems, the system will remain in the spin polarized state. The spinless fermions have been realized in many ex-

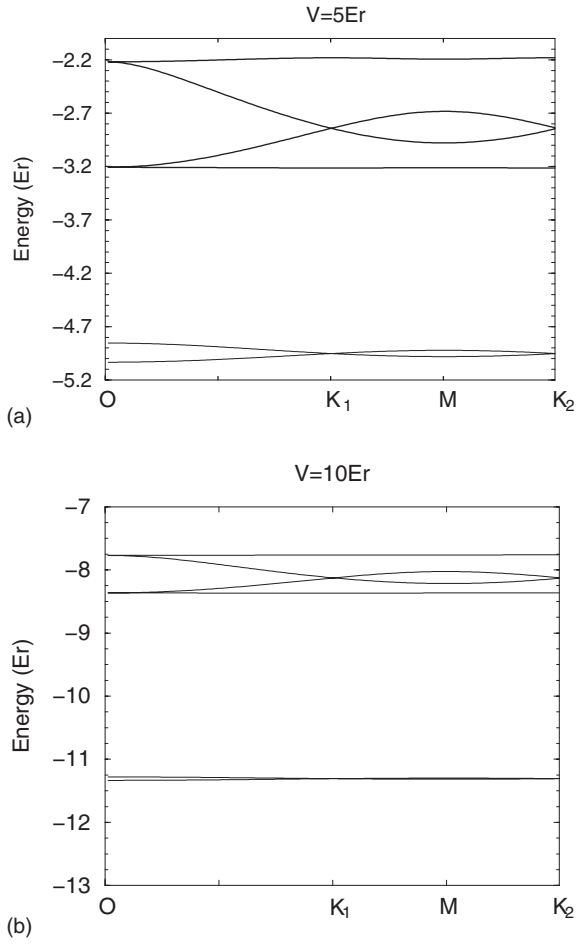

FIG. 8. Band structures for the realistic optical potential in Eq. (1) along the path from $O \to K_1 \to M \to K_2$ in the Brillouin zone with (a) $V/E_r=5$ and (b) $V/E_r=10$.

periments. In particular, the strongly correlated polarized spinless fermion systems have been realized by using the p-wave Feshbach resonance.[33–36] Therefore, in contrast to solid-state electronic systems, where spin is almost always an important quantum dynamical variable, the cold atom fermionic systems created by Feshbach resonance can be prepared as spinless (i.e., spin polarized), and consequently, our current spinless theory applies to such systems without any modifications. Of course, the problem of creating a laboratory $p_{x,y}$-orbital graphene system in cold atomic gases still remains, but given the rapid current experimental developments in fermionic cold atom matter, we are optimistic that our proposed system should soon be realized in practice.

Because of the orbital degeneracy, the on-site interaction for spinless fermions remains Hubbard-type,

$$H_{\text{int}} = U \sum_{\vec{r}} n_{\vec{r},x} n_{\vec{r},y}, \tag{26}$$

where the on-site interaction U is

$$U = \int d\vec{r}_1 d\vec{r}_2 V(\vec{r}_1 - \vec{r}_2) \{ [\psi_{p_x}(\vec{r}_1)\psi_{p_y}(\vec{r}_2)]^2 - [\psi_{p_x}(\vec{r}_1)\psi_{p_y}(\vec{r}_1)\psi_{p_x}(\vec{r}_2)\psi_{p_y}(\vec{r}_2)] \}. \tag{27}$$

Due to Paul's exclusion principle, the s-wave scattering vanishes, and thus the p-wave scattering is the leading-order contribution which is typically weak for low energy particles. The p-band fermions have high kinetic energy, and thus their p-wave scattering might not be small. To enhance U, we can use the p-wave Feshbach resonances among spinless fermions [e.g., ^{40}K (Refs. 33 and 36) and ^{6}Li (Ref. 35)]. Although we do not want the system staying too close to the resonance because of the large atom loss rate there, an enhancement of U to the order of the recoil energy E_R while maintaining the stability of the system is still reasonable.

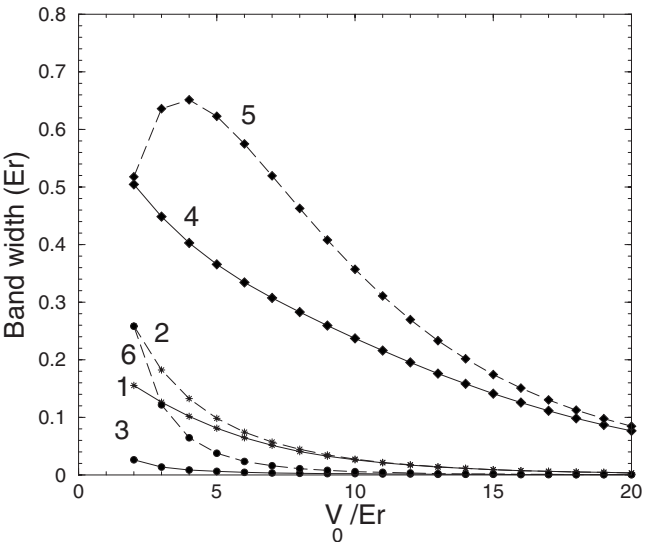

FIG. 9. Width of the beginning six bands of the optical potential in Eq. (1). Bands 1 and 2 are the s-orbital bands. Moreover, bands 3–6 are the $p_{x,y}$-orbital bands, where those of 3 and 6 are flat as discussed before.

Another possible method is to use atoms with large magnetic moments which interact through magnetic-dipole-dipole interactions as

$$V(\vec{r}_1 - \vec{r}_2) = \frac{1}{r^3}\{\vec{m}_1 \cdot \vec{m}_2 - 3(\vec{m}_1 \cdot \hat{r})(\vec{m}_2 \cdot \hat{r})\}, \tag{28}$$

where $r=|\vec{r}_1-\vec{r}_2|$ and $\hat{r}=(\vec{r}_1-\vec{r}_2)/r$. The fermionic atom of ^{53}Cr is a good candidate whose magnetic moment is $m_{\text{Cr}}=6\mu_B$ (Bohr magneton). The spin polarization can be controlled by an external magnetic field. Below we give an estimation of U from the magnetic-dipole interaction. The vibration frequency in each site can be obtained as $\omega_{x,y}=\sqrt{\frac{3}{2}V_0 E_r}$. The length scale of the $p_{x,y}$ orbitals ($l_{x,y}=\sqrt{\hbar/m\omega_{x,y}}$) is typically one order smaller than a. For example, we estimate that $l_{x,y}/a \approx 0.2$ at $V_0/E_r=5$. Assuming strong confinement in the z axis $l_z \ll l_{x,y}$, the vector $\vec{r}_1-\vec{r}_2$ linking two atoms in p_x and p_y orbits almost lies in the xy plane. When the fermion spin is polarized along the z axis, the interaction is repulsive and U can be approximately estimated as

$$U \approx \frac{m_{\text{Cr}}^2}{\langle r^3 \rangle}(1 - 3\langle \cos^2\theta \rangle), \tag{29}$$

where θ is the angle between $\vec{r}_1-\vec{r}_2$ and the z axis. We estimate $\langle r \rangle = \sqrt{2l_{xy}^2 + l_z^2}$ and $\cos\theta = l_z/r$ and find that U can reach

the order of E_r. For example, if we use the laser wavelength $\lambda \approx 0.8$ μm, $V/E_r=5$ (so that $l_{x,y} \approx 0.2a$), and $l_z=0.2l_{x,y}$, we arrive at $U=2.2$ KHz or approximately 100 nK. Increasing V/E_r can further increase U and suppress $t_\parallel$, thus driving the system into an even stronger correlation regime. U can be adjusted from repulsive to attractive by tuning the polarization direction from perpendicular to parallel to the xy plane.

IV. WIGNER-CRYSTAL STATE AT $\frac{1}{6}$ FILLING

In this section, we discuss interaction effects in the $p_{x,y}$-orbital systems. When the flat band is partially filled, interaction effects dominate the physics. In particular, a Wigner-crystal state is stabilized even with the shortest-range on-site interaction. We will mainly study the spinless fermion system below, and also give a brief discussion on the boson systems, but leave the study of the spinful fermion systems to a future publication.

A. Close-packed plaquette state

Due to the complete suppression of the kinetic energy in the flat band, the effect of interactions is nonperturbative when the flat band is partially filled. Interestingly, at sufficiently low particle density $n \leq \frac{1}{6}$, the exact many-body ground state can be easily constructed as follows. Each individual particle localizes into a plaquette state depicted in Fig. 4. Any arrangement of these plaquette states avoiding touching each other is the kinetic-energy ground state and costs zero interaction energy. Since the interaction is repulsive, this class of states also minimizes the interaction energy and thus they constitute the many-body ground states. If we fix the particle density at $n < \frac{1}{6}$, the ground-state configurations have large degeneracy corresponding to all the possible ways to arrange these hard hexagons.

Another class of systems exhibiting similar behavior is the frustrated magnets near full polarization in a large external magnetic field. The Holstein-Primakoff magnons, which are bosons, have a dispersionless flat band over the magnetic Brillouin zone. Interactions among magnons result in the magnon crystal state and magnetization plateau[37] near the full polarization. However, this flat band behavior is difficult to observe because a very strong magnetic field to drive the system close to the full polarization is required. This means that the Zeeman energy reaches the exchange energy J which is typically larger than the order of meV. The flat band phenomenon also appears in systems of "fermion condensation" where strong interactions drive an originally dispersive band to flat within a finite width around the Fermi energy.[38] This has been proposed to explain the Curie law behavior of the magnetic susceptibility in the itinerant heavy fermion compound $CeCoIn_5$ system.[39]

The close-packed plaquette pattern without overlapping each other, is depicted in Fig. 10 corresponding to the filling of $n=\frac{1}{6}$. The completely filled lowest flat band corresponds to $n=\frac{1}{2}$; thus, this close-packed plaquette pattern corresponds to $\frac{1}{3}$ filling of the flat band. This state breaks the lattice translational symmetry and is threefold degenerate. The other two equivalent states can be obtained by translating the state in Fig. 10 along the x axis in the right or left direction at one lattice constant.

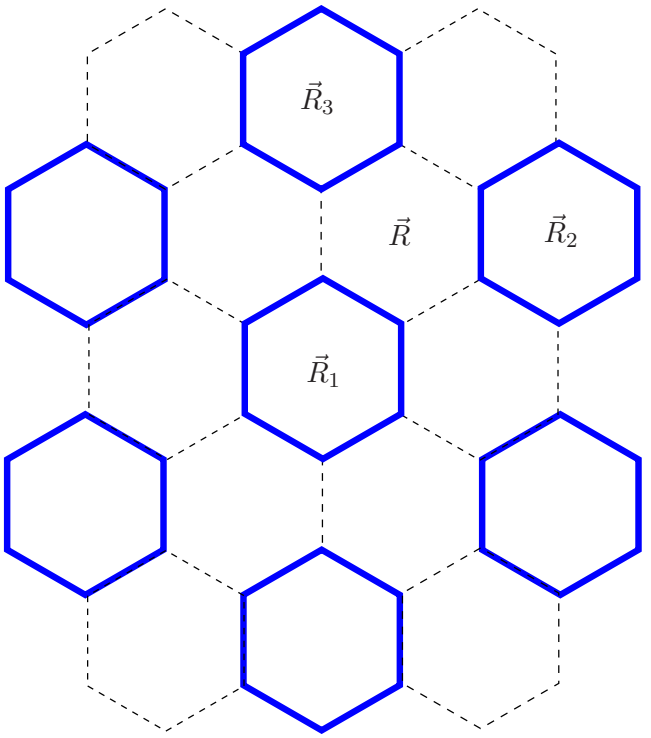

FIG. 10. (Color online) The configuration of the close-packed Wigner-crystal state for both bosons and fermions at $n=\frac{1}{6}$. Each thickened plaquette has the same configuration as in Fig. 4 [from Wu *et al.* (Ref. 19)].

B. Stability of the Wigner-crystal state

The above Wigner-crystal state is a gapped state. We can give a rough estimation for an upper limit of the charge gap by constructing a trial wave function for putting an extra particle in the close-packed state in Fig. 10. In the weak-interaction case $(U/t_\parallel \ll 1)$, we can put the extra atom in the plaquette state located at $\vec{R}$ which is adjacent to three occupied plaquettes $\vec{R}_{1,2,3}$. Since there is already $\frac{1}{6}$ atom on average per site, the cost of the repulsion is $\frac{U}{6}$. On the other hand, in the strong-coupling case $(U/t_\parallel \gg 1)$, we put the particle into an excited state of the occupied plaquette $\vec{R}_1$ while fixing the orbital configuration on each site. Because fermions are spinless, the cost of energy comes from the kinetic part with the value of $\frac{3}{4}t_\parallel$. Thus we obtain the upper limit for the charge gap which is determined by interaction at small values of U and by kinetic energy $t_\parallel$ at large values of U as

$$\Delta < \min\left(\frac{1}{6}U, \frac{3}{4}t_\parallel\right). \tag{30}$$

The above intuitive picture can be made more rigorous by performing a self-consistent mean-field treatment to the Hamiltonian described below.

We decouple Eq. (26) both in the direct and exchange channels as

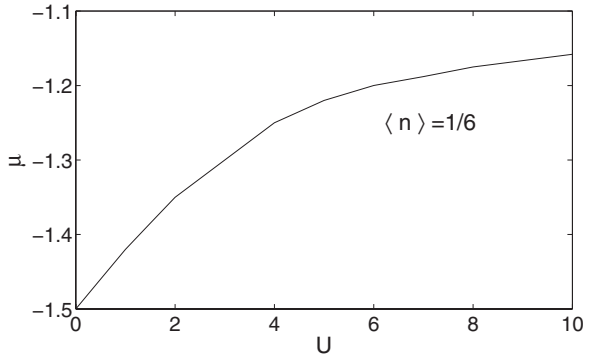

FIG. 11. The phase boundary of the incompressible plaquette Wigner-crystal state of spinless fermions at $\langle n\rangle=\frac{1}{6}$ [from Wu *et al.* (Ref. 19)].

$$H_{\mathrm{mf,int}} = U \sum_{\vec{r}\in A\oplus B} \left\{ n_{\vec{r},x}\left[\frac{\langle n_{\vec{r}}\rangle}{2} - \langle n_{\vec{r},1}\rangle\right] + n_{\vec{r},y}\left[\frac{\langle n_{\vec{r}}\rangle}{2} + \langle n_{\vec{r},1}\rangle\right] - p^{\dagger}_{\vec{r}x} p_{\vec{r}y}[\langle n_{\vec{r},2}\rangle - i\langle n_{\vec{r},3}\rangle] - \mathrm{H.c.}\right\}, \tag{31}$$

$$n_{\vec{r},1} = \frac{1}{2}(p^{\dagger}_{\vec{r}x} p_{\vec{r}x} - p^{\dagger}_{\vec{r}y} p_{\vec{r}y}),$$

$$n_{\vec{r},2} = \frac{1}{2}(p^{\dagger}_{\vec{r}x} p_{\vec{r}y} + \mathrm{H.c.}),$$

$$n_{\vec{r},3} = \frac{1}{2i}(p^{\dagger}_{\vec{r}x} p_{\vec{r}y} - \mathrm{H.c.}), \tag{32}$$

where $n_{1,2,3}$ are the pseudospin operators. $n_{\vec{r},1}, n_{\vec{r},2}$ are time-reversal invariant and describe the preferential occupation of a "dumbbell-shaped" real p-orbital orientation; $n_{\vec{r},3}$ is the orbital angular momentum and is time-reversal odd. We perform a self-consistent mean-field solution to Eq. (31) plus Eq. (5) for the filling level in the range of $\langle n\rangle=0-1$. The self-consistent equation reads

$$\langle n_{\vec{r},i}\rangle = \langle \Omega[\langle n_{\vec{r},j}\rangle]|n_{\vec{r},i}|\Omega[\langle n_{\vec{r},j}\rangle]\rangle \quad (i,j=1-3), \tag{33}$$

where $|\Omega[n_{\vec{r},j}]\rangle$ is the mean-field ground state with the specified configuration of $\langle n_{\vec{r},j}\rangle$.

At the mean-field level, we found that $\langle n_{\vec{r},3}\rangle$ is zero which means the time-reversal symmetry is kept. We need to take an enlarged unit cell to allow the spatial variation of the order parameters. In order to obtain the plaquette order in Fig. 10, this enlarged unit cell covers six sites around a plaquette. We present the range of chemical potential μ for the $\frac{1}{6}$-Wigner-crystal state in Fig. 11, which corresponds to the excitation gap. The charge gap grows roughly linearly with U in the weak-interaction regime and saturates at a value comparable to $t_{\parallel}$ in the strong-interaction regime. Both agree with the above variational analysis.

Next we discuss the effect of the π-bonding term to the $\frac{1}{6}$ state. Such a term gives a width determined by $t_{\perp}$ to the originally flat band. Because the $\frac{1}{6}$ state is gapped, it should remain stable if the band is sufficiently narrow. The plaquette state costs the kinetic energy at the order of $t_{\perp}$ per particle while it saves the repulsive interaction at the order of $\frac{U}{6}$. Thus for small values of $t_{\perp}$, a stability condition of this state can therefore be roughly estimated as $U>6t_{\perp}$. We have checked this numerically. For example, setting $t_{\perp}/t_{\parallel}=0.1$, we find that the $\frac{1}{6}$ state survives $U>t_{\parallel}$. In realistic systems, the ratio of $t_{\perp}/t_{\parallel}$ is much smaller than 0.1 with reasonable values of V/E_r, as shown in Fig. 9; thus, the $\frac{1}{6}$ state can be stabilized at much smaller values of U.

C. Bosonic Wigner-crystal state

In the above hard hexagon state at $n=\frac{1}{6}$, particles are separated from each other; thus, particle statistics do not play any role. Such a Wigner-crystal state should also occur with bosons or Bose-Fermi mixtures with repulsive interactions. The on-site interaction for p-band bosons reads

$$H_{\mathrm{int}} = \frac{U}{2}\sum_{\vec{r}} \left\{ n^2_{\vec{r}} - \frac{1}{3} L^2_{z,\vec{r}} \right\}, \tag{34}$$

where n is the total particle number and L_z is the orbital angular momentum.[9,11] The p-band bosonic systems have been created experimentally.[18] The lifetime of the p-band bosons is significantly enhanced when the particle density per site is less than 1, which can be hundreds of times longer than the hopping timer from one site to its neighbors. Thus the $\frac{1}{6}$ state is also experimentally feasible in bosonic systems.

V. CHARGE AND BOND ORDERINGS AT COMMENSURATE FILLINGS OF $n>\frac{1}{6}$

In this section, we investigate the charge and bond orderings at commensurate fillings higher than $\frac{1}{6}$ by using the mean-field theory to solve the interacting Hamiltonian self-consistently. We will present the result in both weak- and strong-coupling regimes but leave the detailed investigation of the physics of orbital exchange at $n=1$ to future research. In the following calculation, we confine ourselves to the unit cell of up to six sites.

A. Weak-coupling regime

When the filling $n>\frac{1}{6}$, exact solutions are no longer available. Again we perform the self-consistent mean-field solution to the interacting Hamiltonian. In the weak-coupling regime ($U/t_{\parallel}=1$), we plot the relation of the filling $\langle n\rangle$ vs μ in Fig. 12(a). As μ passes the charge gap, the system enters a compressible state. $\langle n\rangle$ increases with μ quickly with a finite but large slope. This means that particles fill in other states in the flat band. Due to the pre-existing crystalline ordered background, these states are no longer exactly flat and develop weak dispersions. This corresponds to adding additional $\frac{N}{6}$ particles into the background of the $\frac{1}{6}$ state, as depicted in Fig. 10 (N—the total number of lattice sites). Roughly speaking, these particles also go into the localized plaquette states. When $\langle n\rangle\approx\frac{1}{3}$, we see a significant reduction in density of states compared to those of the flat band, which still has a finite density of state attributed to the filling of the dispersive band.

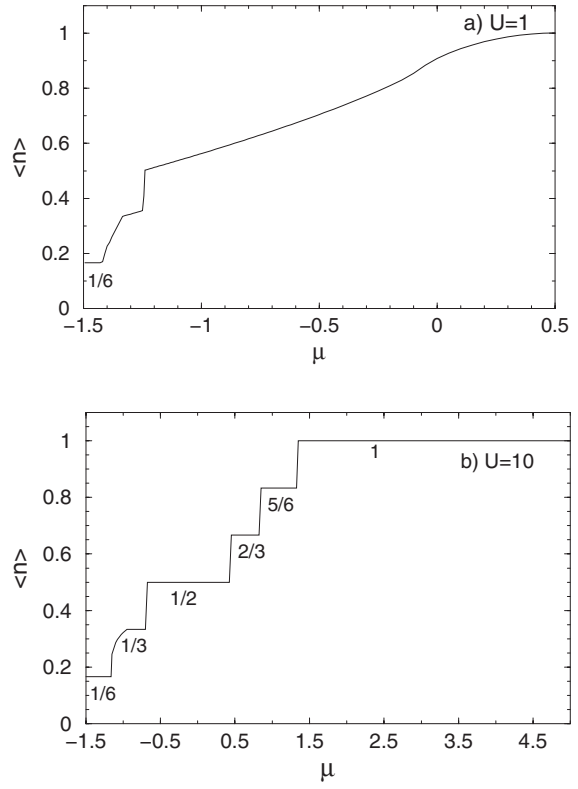

FIG. 12. The filling $\langle n\rangle$ vs the chemical potential μ for spinless fermions for (a) weak and (b) strong interactions. Due to the particle-hole symmetry, only the part with μ from the band bottom $-\frac{3}{2}t_{\|}$ to $U/2$ is shown. Only one plateau appears in (a) at $n=\frac{1}{6}$, while a series of plateaus appears in (b) at $n=\frac{1}{6}$, $\frac{1}{3}$, $\frac{1}{2}$, $\frac{2}{3}$, $\frac{5}{6}$, and 1 [from Wu *et al.* (Ref. 19)].

Let us look at the quasiplateau at $\langle n\rangle \approx \frac{1}{3}$. Although these occupied plaquettes can be arranged to avoid each other as we did before, they unavoidably will touch the preoccupied ones. As a result, for each occupied plaquette state, three of its six neighbors are occupied alternatively. The orbital configuration in such a state is as depicted in Fig. 13; for each bond shared by two occupied plaquettes, the p-orbital orientation is parallel to the bond direction as a compromise between two neighboring plaquettes. The bonding strength exhibits a dimerized pattern. The ratio between the weakened and strengthened bonds is approximately 0.44. Compared to the gapped dimerized phase that will be discussed below in Sec. V B, this is a relatively weakly dimerized phase.

At $\langle n\rangle > \frac{1}{2}$, all the flat band states are completely filled. In the weak-coupling regime, interaction effects are no longer important and crystalline orders vanish. Near $\langle n\rangle = 1$, the density of states becomes linear with energy as controlled by the Dirac cones. Recently, it has been proposed to use the s band in the honeycomb optical lattice to simulate the Dirac cone physics.[40] The $p_{x,y}$-band Dirac cones described above are also good for this purpose and have even more advantages. The velocity of the $p_{x,y}$-Dirac cone is much larger than that of the s band due to a much larger bandwidth, as shown in Fig. 9. The large energy scale here renders quantum degeneracy and the low-temperature regime much more accessible.

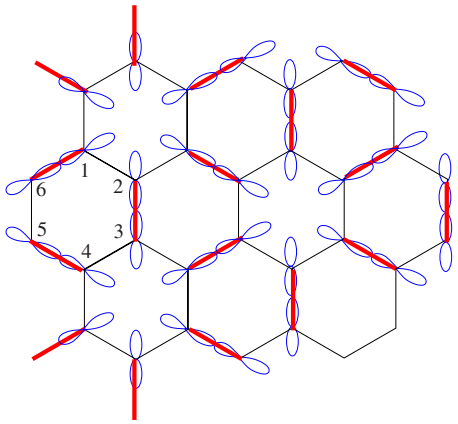

FIG. 13. (Color online) Bonding strength dimerization can occur at both $\langle n\rangle = \frac{1}{3}$ in the weak-coupling regime and $\langle n\rangle = \frac{1}{2}$ in the strong-coupling regime as depicted by the thickened (red) bonds. The orbital orientation in the dimer is along the bond direction. In the weak-coupling case ($\langle n\rangle = \frac{1}{3}$), the thickened bonds correspond to the shared edges of two neighboring plaquette states in the flat band. In the strong-coupling case ($\langle n\rangle = \frac{1}{2}$), each dimer contains one particle as an entangled state of occupied and empty sites.

B. Strong-coupling regime at $n > \frac{1}{6}$

The physics in the strong-coupling regime is very different from that in the weak-coupling regime. Much more crystalline ordered states appear in the strong-coupling regime at commensurate fillings exhibiting rich structures of dimerization and trimerization orders. The relation of the filling $\langle n\rangle$ vs μ at $U/t=10$ is depicted in Fig. 12(b). A series of plateaus occurs at commensurate fillings of $\langle n\rangle = \frac{i}{6}$ $(i=1-6)$, which correspond to a set of charge and bond ordered insulating states. The charge gap for each insulating state is at the order of $t_{\|}$ except for that at $\langle n\rangle = 1$ which is at the order of U. Since these gapped states appear at the strong-interaction regime, they are not sensitive to a small $t_{\perp}$. The band structure described in Secs. I–IV is completely changed by the strong interactions. Roughly speaking, at $\langle n\rangle > \frac{1}{6}$, the preoccupied plaquette states exert strong effects to the extra particles and vice versa. The remaining part of the flat band disappears and the Dirac cone structure is also destroyed.

At $\langle n\rangle = \frac{1}{3}$, the strong-coupling crystalline ordering pattern is different from that in the weak-coupling regime depicted in Fig. 13. The system exhibits a trimerized pattern, as depicted in Fig. 14. Each trimer is repented as two thickened bonds and contains one particle. In other words, each hexagon plaquette in the $\langle n\rangle = \frac{1}{6}$ case is occupied by two particles. Such a state is also threefold degenerate, and the other two equivalent states can be obtained by translating the system one lattice constant to the right and left directions. Let us consider one plaquette unit cell and describe the orbital configuration. We mark the six sites as 1–6. The p-orbital configurations at sites 1, 6, and 2 are p_x, $\cos\theta p_x \pm \sin\theta p_y (\theta = 158.4°)$, and those at 4, 5, and 3 are related by a reflection operation with respect to the x axis. In other words, the occupied p orbital at site 1 is parallel to the x axis and that at site 6 is almost along the direction of bond (1,6) with a small deviation of 8.4°. The particle densities at each site are

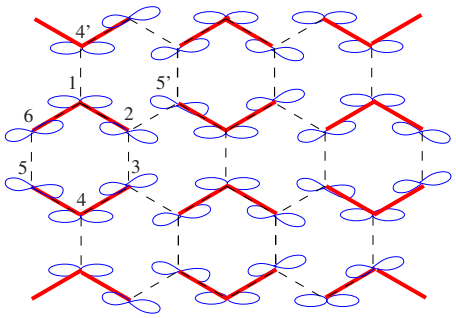

FIG. 14. (Color online) The trimerized states at fillings $\langle n\rangle = \frac{1}{3}, \frac{2}{3}$ in the strong-coupling regime as described by thickened bonds. Each trimer contains one particle at $\langle n\rangle = \frac{1}{3}$ and two particles at $\langle n\rangle = \frac{2}{3}$.

$n_{6,2,3,5}=0.27$ and $n_{1,4}=0.46$. The bonding strength between neighboring sites i,j is defined as $B_{ij}=-\langle(p_i^\dagger \hat{e}_{ij})(p_j \hat{e}_{ij}) + \text{H.c.}\rangle$. There are four nonequivalent bond strengths: $(i,j)=(2,1)$, $(2,3)$, $(2,5')$, and $(1,4')$, where $4'$ and $5'$ are the equivalent sites of 4 and 5 in the neighboring plaquettes. We have $B_{2,1}=0.58t_\parallel$, $B_{2,3}=0.04t_\parallel$, $B_{2,5'}=0.14t_\parallel$, and $B_{1,4'}=0$. The average bonding energy per site can be evaluated from the above bonding strengths as $0.446t_\parallel$. Instead of the above trimer pattern, one might also think of the dimer covering with filling $\frac{1}{3}$ in which only two-third of the sites are covered by dimers. However, a rough estimation of the average bonding energy per site is approximately $\frac{1}{3}t_\parallel$, which is less energetically favorable because particles are more localized in the dimer configuration.

The crystalline order pattern at the filling of $\langle n\rangle = \frac{2}{3}$ is similar to that at $\langle n\rangle = \frac{1}{3}$ with each trimer containing two particles. In this case, the parameters above change to $\theta=153°$, $n_{6,2,3,5}=0.76$ and $n_{1,4}=0.49$, and $B_{2,1}=0.70t_\parallel$, $B_{2,3}=0.07t_\parallel$, $B_{2,5'}=0.12t_\parallel$, and $B_{1,4'}=0.02t_\parallel$.

At $\langle n\rangle = \frac{1}{2}$, the system exhibits a dimerized pattern similar to that of $\langle n\rangle = \frac{1}{3}$ in the weak-coupling regime, as illustrated in Fig. 13. The major difference is that the dimerized state here is an incompressible insulating state while that in the weak-coupling regime is with a small but still nonvanishing compressibility. The dimer is represented by a thickened bond in which one particle hops back and forth. It can be considered as a superposition of the two states of two sites where one is occupied and the other is empty. There are only two nonequivalent bonding strengths: $B_{1,6}=0.95t_\parallel$ and $B_{1,2}=0.1t_\parallel$. The former is about one order larger that the latter, thus the system is in the strong dimerization limit. As shown in Fig. 12(b), the energy scale of this dimerized phase is set by $t_\parallel$, which is much larger than the usual one in dimerized magnetic systems with $t_\parallel^2/U$.

The low energy physics in the dimer phase should be described by a quantum dimer model,[41] which includes the quantum resonance of different patterns of dimer coverings. Although in the physical parameter regime the dimer crystal configuration in Fig. 13 is stabilized, it would be interesting to further investigate how to enhance quantum fluctuations to achieve the quantum disordered dimer liquid phase. The corresponding possible orbital liquid state in the $p_{x,y}$-orbital systems would be an exciting state for a future study.[6]

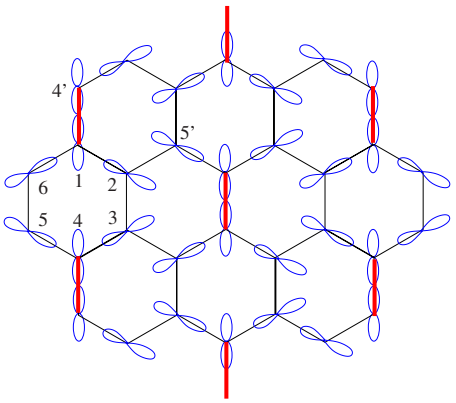

FIG. 15. (Color online) The orbital configuration at the filling $\langle n\rangle = \frac{5}{6}$ exhibits the dimerized state of holes in the strong-coupling regime. The holes mainly distribute on the position of sites 1 and 4 in each unit cell with a large bonding strength.

The ordering pattern at another commensurate filling of $\langle n\rangle = \frac{5}{6}$, as shown in Fig. 15. The p-orbital configurations at sites 1, 6, and 2 are p_y, $\cos\theta p_x \pm \sin\theta p_y$ with $\theta=150.2°$, and those at 4, 5, and 3 are related by a reflection operation with respect to the x axis. The particle densities at each site are $n_{6,2,3,5}=0.94$ and $n_{1,4}=0.62$. The four nonequivalent bond strengths read $B_{2,1}=0.36$, $B_{2,3}=0.08$, $B_{2,5'}=0.08$, and $B_{1,4'}=0.83$. The $\frac{5}{6}$-filling state can be considered as doping the insulating state of one particle per site with $\frac{1}{6}$ holes. Holes are mainly concentrated on the positions of sites 1 and 4 in each unit cell. The corresponding bonds have the largest bonding strength. Such a state is the dimerized state of holes.

VI. TIME-OF-FLIGHT SPECTRA

Noise correlation has become an important method to detect the ordering in cold atom systems in optical lattices.[42,43] In all the Mott-insulating states at commensurate fillings described in Figs. 10 and 13–15, the enlarged unit cell contains six sites forming a plaquette. They should exhibit themselves in the noise correlation of the TOF signals. In the presence of the charge and bond orders, the reciprocal wave vectors of the reduced Brillouin zone become $\vec{G}_1' = (\frac{4\pi}{3\sqrt{3}a}, 0) = \frac{-1}{3}\vec{G}_1 + \frac{2}{3}\vec{G}_2$ and $\vec{G}_2' = (\frac{-2\pi}{3\sqrt{3}a}, \frac{2\pi}{3a}) = \frac{2}{3}\vec{G}_1 - \frac{1}{3}\vec{G}_2$, where $\vec{G}_{1,2}$ are the reciprocal wave vectors for the original Brillouin zone. The correlation function is defined as

$$C_t(\vec{r},\vec{r}') = \langle n(\vec{r})n(\vec{r}')\rangle_t - \langle n(\vec{r})\rangle_t\langle n(\vec{r}')\rangle_t, \tag{35}$$

where t is the flying time.

For the close-packed hexagon state at $\langle n\rangle = \frac{1}{6}$, Eq. (35) can be easily calculated. We have $\langle n(\vec{r})_t\rangle = (\frac{m}{\hbar t})^3 |\psi(\vec{k})|^2$, where $\vec{k} = m\vec{r}/(\hbar t)$ and $\psi(\vec{k})$ is the Fourier transform of the plaquette-Wannier state depicted in Fig. 4. Thus

$$C_t(\vec{r},\vec{r}') = \mp \frac{N}{6}\left(\frac{m}{\hbar t}\right)^6 |\psi(\vec{k})|^2 |\psi(\vec{k}')|^2 \sum_{\vec{G}'} \delta(\vec{k} - \vec{k}' - \vec{G}'), \tag{36}$$

where $-$ $(+)$ is for fermions (bosons), respectively, $\vec{G}' = m\vec{G}_1' + n\vec{G}_2'$ with m,n integers, and $\vec{k}' = m\vec{r}'/(\hbar t)$. After a spatial averaging and normalization, we find

$$C_t(\vec{d}) = \int d\vec{r} \frac{C_t\left(\vec{r}+\frac{\vec{d}}{2},\vec{r}-\frac{\vec{d}}{2}\right)}{\left\langle n\left(\vec{r}+\frac{\vec{d}}{2}\right)\right\rangle_t \left\langle n\left(\vec{r}-\frac{\vec{d}}{2}\right)\right\rangle_t} \propto \mp \sum_{\vec{G}'} \delta(\vec{k}-\vec{G}'), \tag{37}$$

where $\vec{k}=m\vec{d}/(\hbar t)$. All the δ peaks are with equal weight because of the cancellation of the Fourier transform of the Wannier function and the sixfold rotational symmetry in Fig. 4.

For the crystalline ordering of fermions at other commensurate fillings, the noise correlation functions still exhibit the δ peaks located at the same reciprocal wave vectors of the reduced Brillouin zone. However, the form factors are more complicated. Generally, $\langle n(\vec{r})\rangle$ and $C_t(\vec{r},\vec{r}')$ can be calculated as

$$\langle n(\vec{r})_t\rangle \propto \sum_{\mu\nu} \psi^*_\mu(\vec{k})\psi_\nu(\vec{k})\langle\Omega|p^\dagger_\mu(\vec{k})p_\nu(\vec{k})|\Omega\rangle,$$

$$C_t(\vec{r},\vec{r}') \propto -\left|\sum_{\mu\nu} \psi^*_\mu(\vec{k})\psi_\nu(\vec{k}')\langle\Omega|p^\dagger_\mu(\vec{k})p_\nu(\vec{k}')|\Omega\rangle\right|^2 \times \sum_{\vec{G}'} \delta(\vec{k}-\vec{k}'-\vec{G}'), \tag{38}$$

where the Greek indices μ and ν denote the Wannier functions for the 12 $p_{x,y}$ orbitals in one plaquette. In particular, due to the loss of the sixfold lattice rotational symmetry in Figs. 14 and 15, the noise spectra of $C_t(\vec{d})$ should show the reduced twofold rotational symmetry. Figure 13 still keeps the sixfold rotational symmetry, but the weight of the δ functions should not be the same as in Eq. (37).

VII. CONCLUSION AND DISCUSSION

In summary, we have proposed the laboratory analog simulation of a kind of artificial graphene, unavailable in nature, where the $p_{x,y}$ orbitals are the key, unlike the real graphene made of the p_z orbital. This switching of orbitals, as shown in this work, leads to strong correlation physics which cannot be studied in the corresponding solid-state graphene systems.

We have shown that the band structure of $p_{x,y}$-orbital honeycomb lattices contains both Dirac cones and flat bands. Particle interactions stabilize various incompressible Wigner-crystal-like states at commensurate fillings. In particular, we have described the exact many-body ground state at $\langle n\rangle=\frac{1}{6}$, which exhibits close-packed hexagon plaquette order. Various charge and bond orderings appear in the strong-coupling regime at higher commensurate fillings. These states exhibit their patterns in the noise correlation of time-of-flight experiments. Taking into account the recent exciting experimental realization of the p-orbital bosons[18] and the fact that the honeycomb optical lattices were experimentally constructed quite some time ago,[32] the $p_{x,y}$-orbital counterpart of graphene may be achieved in the laboratory in the near future.

Let us compare the Wigner-crystal states in the $p_{x,y}$-orbital systems with those in the electron-gas systems. Quantum Monte Carlo simulations show that the Wigner-crystal state is stable in the very low-density regime at $r_s>39$ in two dimensions, where r_s is the ratio between the average interelectron distance and the Bohr radius.[27] The long-range Coulomb interactions dominate over the kinetic energy when r_s is large. In contrast, even the shortest-range repulsive interaction can stabilize the crystal state in the $p_{x,y}$-orbital honeycomb lattice due to the suppression of the kinetic energy by the band flatness. The Wigner-crystal state also occurs in the fractional quantum Hall systems due to the suppression of kinetic energy by the magnetic field.[44,45] At low filling factors, crystalline ordered states energetically win over the Laughlin liquid state. It is also interesting to note the difference between our system and the p_z-orbital system of graphene, where the characteristic ratio between Coulomb interaction and kinetic energy $\frac{e^2}{\hbar v_f}$ (v_f is the slope of the Dirac cone) is a constant independent of charge-carrier density. As pointed out in Refs. 28, 31, and 46, interactions in graphene are not strong enough to stabilize the Wigner-crystal state at any density.

Many interesting problems still remain open for further exploration, and we will leave them to future publications. For example, for the spinful fermions with repulsive interactions, it is natural to expect ferromagnetism due to the flat band structure. It would be interesting to study the competition between antiferromagnetic exchange and flat band ferromagnetism. If interactions are attractive, the pairing problem and the corresponding BCS-BEC crossover in the flat band might prove interesting. On the other hand, if we load bosons into the flat band beyond the density of $\langle n\rangle=\frac{1}{6}$, the frustration effect due to the band flatness to the superfludity is a challenging problem. Most intriguing is the possibility of exotic incompressible states analogous to the Laughlin liquid in the fractional quantum Hall effect. These cannot be captured within the mean-field approximation used here for $n>\frac{1}{6}$. If one could devise appropriate variational liquid states projected into the flat band, these could be compared energetically with the Wigner crystals found here. Given the richness and surprises encountered in the fractional quantum Hall effect, flat band physics in optical lattices appears rife with possibility.

ACKNOWLEDGMENTS

C.W. thanks L. M. Duan, E. Fradkin, and T. L. Ho for helpful discussions, and especially L. Balents and D. Bergman for an early collaboration. C.W. was supported by the start up funding at University of California, San Diego and the Sloan Research Foundation. S.D.S. is supported by ARO-DARPA.

[1] M. H. Anderson, J. R. Ensher, M. R. Matthews, C. E. Wieman, and E. A. Cornell, Science **269**, 198 (1995).
[2] K. Davis, M. Mewes, M. Joffe, M. Andrews, and W. Ketterle, Phys. Rev. Lett. **74**, 5202 (1995).
[3] M. Greiner, O. Mandel, T. W. Hansch, and I. Bloch, Nature (London) **419**, 51 (2002).
[4] M. Imada, A. Fujimori, and Y. Tokura, Rev. Mod. Phys. **70**, 1039 (1998).
[5] Y. Tokura and N. Nagaosa, Science **288**, 462 (2000).
[6] G. Khaliullin, Prog. Theor. Phys. Suppl. **160**, 155 (2005).
[7] V. W. Scarola and S. Das Sarma, Phys. Rev. Lett. **95**, 033003 (2005).
[8] A. Isacsson and S. M. Girvin, Phys. Rev. A **72**, 053604 (2005).
[9] W. V. Liu and C. Wu, Phys. Rev. A **74**, 013607 (2006).
[10] A. B. Kuklov, Phys. Rev. Lett. **97**, 110405 (2006).
[11] C. Wu, W. V. Liu, J. E. Moore, and S. Das Sarma, Phys. Rev. Lett. **97**, 190406 (2006).
[12] C. Xu and M. P. A. Fisher, Phys. Rev. B **75**, 104428 (2007).
[13] C. Xu, arXiv:0706.1609 (unpublished).
[14] O. E. Alon, A. I. Streltsov, and L. S. Cederbaum, Phys. Rev. Lett. **95**, 030405 (2005).
[15] A. Browaeys, H. Haffner, C. McKenzie, S. L. Rolston, K. Helmerson, and W. D. Phillips, Phys. Rev. A **72**, 053605 (2005).
[16] M. Kohl, H. Moritz, T. Stoferle, K. Gunter, and T. Esslinger, Phys. Rev. Lett. **94**, 080403 (2005).
[17] J. Sebby-Strabley, M. Anderlini, P. S. Jessen, and J. V. Porto, Phys. Rev. A **73**, 033605 (2006).
[18] T. Muller, S. Folling, A. Widera, and I. Bloch, Phys. Rev. Lett. **99**, 200405 (2007).
[19] C. Wu, D. Bergman, L. Balents, and S. Das Sarma, Phys. Rev. Lett. **99**, 070401 (2007).
[20] C. Wu, Phys. Rev. Lett. **100**, 200406 (2008).
[21] K. Wu and H. Zhai, Phys. Rev. B **77**, 174431 (2008).
[22] E. Zhao and W. V. Liu, Phys. Rev. Lett. **100**, 160403 (2008).
[23] K. S. Novoselov, A. K. Geim, S. V. Morozov, D. Jiang, M. I. Katsnelson, I. V. Grigorieva, S. V. Dubonos, and A. A. Firsov, Nature (London) **438**, 197 (2005).
[24] Y. Zhang, Y.-W. Tan, H. Stormer, and P. Kim, Nature (London) **438**, 201 (2005).
[25] A. H. Castro Neto, F. Guinea, N. M. R. Peres, K. S. Novoselov, and A. K. Geim, arXiv:0709.1163, Rev. Mod. Phys. (to be published).
[26] H. J. Choi, D. Roundy, H. Sun, M. L. Cohen, and S. G. Louie, Nature (London) **418**, 738 (2002).
[27] B. Tanatar and D. M. Ceperley, Phys. Rev. B **39**, 5005 (1989).
[28] S. Das Sarma, B. Y.-K. Hu, E. H. Hwang, and W.-K. Tse, arXiv:0708.3239 (unpublished).
[29] E. H. Hwang, Ben Yu-Kuang Hu, and S. Das Sarma, Phys. Rev. Lett. **99**, 226801 (2007).
[30] S. Das Sarma, E. H. Hwang, and W. K. Tse, Phys. Rev. B **75**, 121406(R) (2007).
[31] W.-K. Tse and S. Das Sarma, Phys. Rev. Lett. **99**, 236802 (2007).
[32] G. Grynberg, B. Lounis, P. Verkerk, J. Y. Courtois, and C. Salomon, Phys. Rev. Lett. **70**, 2249 (1993).
[33] J. P. Gaebler, J. T. Stewart, J. L. Bohn, and D. S. Jin, Phys. Rev. Lett. **98**, 200403 (2007).
[34] C. A. Regal, C. Ticknor, J. L. Bohn, and D. S. Jin, Phys. Rev. Lett. **90**, 053201 (2003).
[35] J. Zhang, E. G. M. van Kempen, T. Bourdel, L. Khaykovich, J. Cubizolles, F. Chevy, M. Teichmann, L. Tarruell, S. J. J. M. F. Kokkelmans, and C. Salomon, Phys. Rev. A **70**, 030702(R) (2004).
[36] C. Ticknor, C. A. Regal, D. S. Jin, and J. L. Bohn, Phys. Rev. A **69**, 042712 (2004).
[37] M. E. Zhitomirsky and H. Tsunetsugu, Prog. Theor. Phys. Suppl. **160**, 361 (2005).
[38] V. A. Khodel and V. R. Shaginyan, JETP Lett. **51**, 533 (1990).
[39] V. A. Khodel, M. V. Zverev, and V. M. Yakovenko, Phys. Rev. Lett. **95**, 236402 (2005).
[40] S.-L. Zhu, B. Wang, and L. M. Duan, Phys. Rev. Lett. **98**, 260402 (2007).
[41] D. S. Rokhsar and S. A. Kivelson, Phys. Rev. Lett. **61**, 2376 (1988).
[42] E. Altman, E. Demler, and M. D. Lukin, Phys. Rev. A **70**, 013603 (2004).
[43] A. Imambekov, V. Gritsev, and E. Demler, in Proceedings of the 2006 Enrico Fermi Summer School on "Ultracold Fermi Gases", Varenna, Italy, June 2006, edited by M. Inguscio, W. Ketterle, and C. Salomon (unpublished).
[44] Y. P. Chen, G. Sambandamurthy, Z. H. Wang, R. M. Lewis, L. W. Engel, D. C. Tsui, P. D. Ye, L. N. Pfeiffer, and K. W. West, Nat. Phys. **2**, 452 (2006).
[45] P. D. Ye, L. W. Engel, D. C. Tsui, R. M. Lewis, L. N. Pfeiffer, and K. West, Phys. Rev. Lett. **89**, 176802 (2002).
[46] H. P. Dahal, Y. N. Joglekar, K. S. Bedell, and A. V. Balatsky, Phys. Rev. B **74**, 233405 (2006).